Research Article

A method to determine winding losses in integrated inductors and separate skin and proximity effects

A. Abderahim[1] · M. Koularambaye[1] · J. P. Chatelon[1] · S. Capraro[1] · D. Piétroy[1] · J. J. Rousseau[1]

Abstract

This paper presents a method to determine winding losses from scattering matrix parameters in planar inductors. Winding losses are taken into account by a dependent frequency resistance. This method allows losses to be separated in two parts for coreless inductors: skin effect and proximity effect. In high frequencies both software, like High Frequency Structure Simulator, and equipment, like Vector Network Analyzer, provide scattering parameters that allow both impedance or admittance matrices to be calculated. Then, parameters of an electric equivalent circuit can be calculated. The resistance value taking into account both skin and proximity effects is determined in three frequency domains. The first domain is at very low frequencies or at direct current. The second domain is at low-medium frequencies where the capacitive couplings are negligible. The last domain is at the resonant frequencies of the admittance matrix parameters, so at high frequencies. The presented approach is different from those encountered in literature and allows the series resistance from measured or simulated scattering matrix parameters to be determined.

1 Introduction

Power supplies for embedded equipment require high efficiencies, both low weights and sizes. For some years, there has been a strong demand for miniaturization and integration of magnetic components like inductors and transformers for DC–DC power converters. In order to reach high efficiencies, both losses in active and passive components have to be reduced. This article deals with the determination of copper losses versus frequency in integrated magnetic components. Copper losses are modeled by using a serial resistance $r_{(f)}$ that depends on the frequency. The resistance $r_{(f)}$ takes into account both skin and proximity effects. In addition, our approach makes it possible to separate skin and proximity effects. In the past, numerous works were devoted to determination,

calculation of copper losses for wound windings using round wires, Litz wires or foils [1–4]. Some authors investigated winding losses in low-profile magnetic components [5].

Papers related to determination of winding losses in integrated inductors are not so many [6–12]. The analytical expression (1) proposed by Yue [6] which takes into account skin effects is used by most authors.

$$R_{ep} = L \frac{\rho}{w\delta\left(1 - e^{-t/\delta}\right)} \tag{1}$$

R_{ep} series resistance, **L** length of the wire, **ρ** copper resistivity, **w** conductor width, **δ** skin depth, **t** conductor thickness.

On the other hand, Kuhn [7] studied ac winding losses in planar spiral inductors on silicon. They expressed the AC

resistance as a function of the DC resistance and a critical pulsation ω_{cri}:

$$R_{AC} = R_{DC} \left[1 + \frac{1}{10} \left(\frac{\omega}{\omega_{crit}} \right)^2 \right] \qquad (2)$$

$$\omega_{crit} = \frac{3,1(w+s)}{\mu_0 w^2} R_{square} \quad R_{square} = \frac{\rho}{t} \quad \text{and} \quad \omega = 2\pi f$$

s space between two consecutive turns, **f** frequency.

In order to take into account both skin and proximity effects, the pulsation ω_{crit} depends on ω and s.

This expression has been used by some other authors [8]. Otherwise, to take into account both skin and proximity effects some authors have shown how to determine from simulation [9] or from measurement [10] copper losses by using a series resistor. Harburg [11] have modeled AC losses and compared them with 3D simulations. A new approach to calculate copper losses by using a 2D distribution of the magnetic field was also developed [12]. These various methods underconsider or overestimate strongly the losses and they cannot be applied to every component working at high frequency.

So, a method has been developed in order to determine the losses in integrated components. This method has been succinctly presented in [13, 14]. In this article, the developed method is presented in detail and compared with several integrated coreless inductors where the serial resistance of integrated components is determined from measurement or from simulation.

The resistance extraction at low frequencies is obtained very exactly. However, beyond some tens of MHz, it is impossible to measure exactly the resistance using an impedance analyzer. A solution consists in substituting the two-port current–voltage approach by an approach based upon scattering parameters. Thus, only scattering parameters can be obtained by using a Vector Network Analyzer (VNA). Software solutions based on finite element such as High Frequency Structure Simulator (HFSS) also calculate scattering parameters. Well known equations are available to convert S_{ij} parameters into Y_{ij} or Z_{ij} parameters [15].

In this article, coreless inductors (Fig. 1) are chosen in order to have only the resistance parameter which depends on the frequency and allow the developed method to be validated. Afterward, this method can be used for integrated inductors with magnetic material.

Several authors [16–21] modelled the planar inductors by an RLC electrical circuit. Figure 2 shows a coreless inductor model: L is the inductance, C_1 and C_2 represent the capacitive coupling between the spiral and the ground plane and C_{12} takes into account the capacitive coupling between turns. The only resistance $r_{(f)}$ is depending on
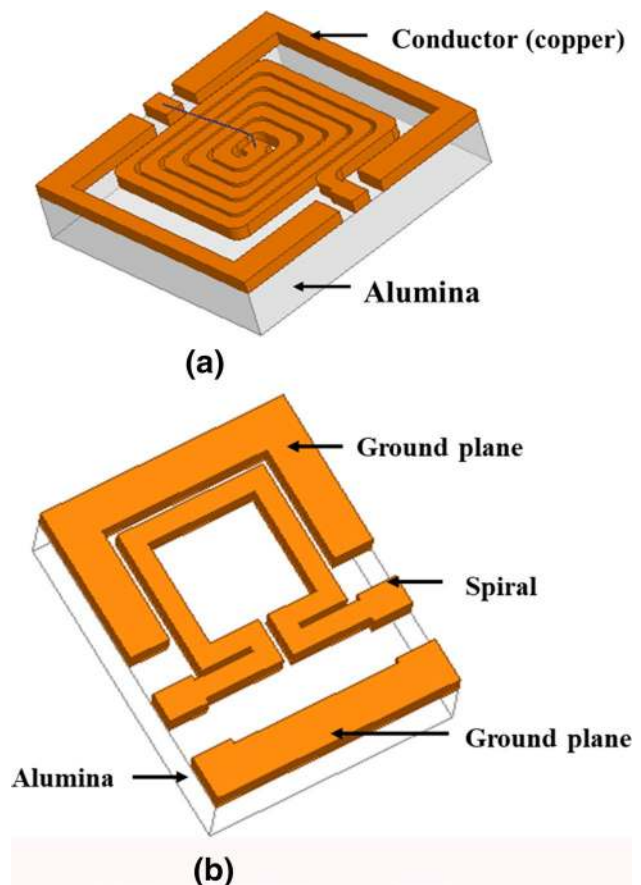

Fig. 1 Coreless inductors, **a** spiral inductor with 5 turns **b** spiral inductor with 1 turn

the frequency in order to model both skin and proximity effects.

2 Determination of the model parameters

2.1 Equivalent electrical circuit

Inductors are considered as a two-port network (Fig. 3). They are usually expressed in matrix notation which establishes relations between the current–voltage variables:

V_1 voltage across port 1, I_1 current into port 1, V_2 voltage across port 2 and I_2 current into port 2.

The relationship between the port voltages, port currents and the Y-parameter matrix is given by:

$$\begin{bmatrix} I_1 \\ I_2 \end{bmatrix} = \begin{bmatrix} Y_{11} Y_{12} \\ Y_{21} Y_{22} \end{bmatrix} \begin{bmatrix} V_1 \\ V_2 \end{bmatrix} \quad \begin{cases} I_1 = Y_{11} \cdot V_1 + Y_{12} \cdot V_2 \\ I_2 = Y_{21} \cdot V_1 + Y_{22} \cdot V_2 \end{cases} \qquad (3)$$

Four constant elements (L, C_1, C_2 and C_{12}) and one frequency dependent, r, parameters have to be determined.
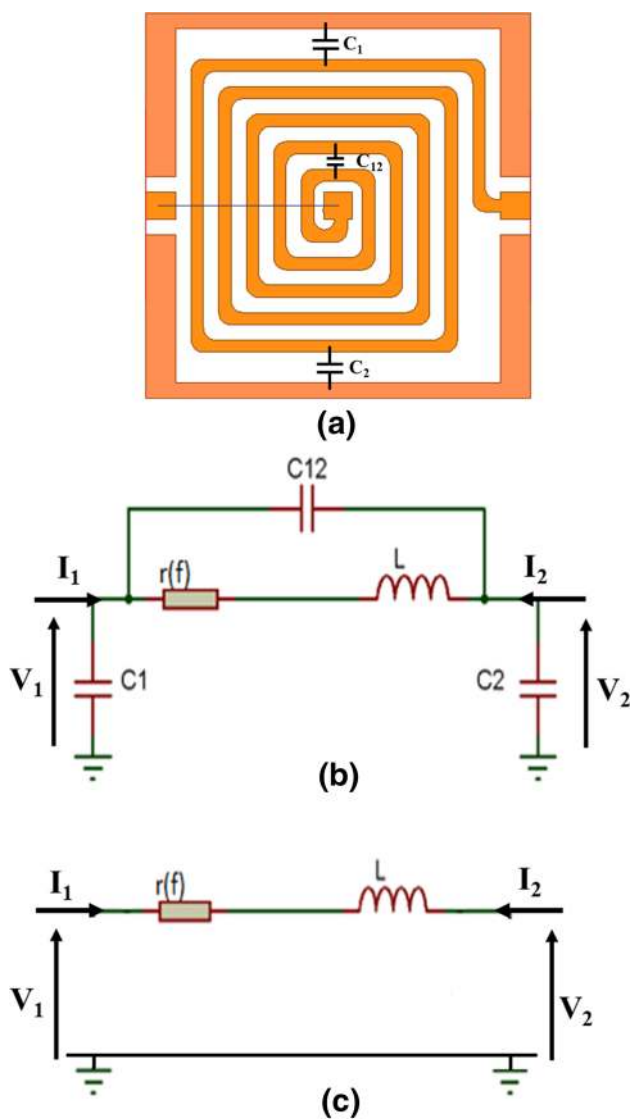
(a)

(b)

(c)

Fig. 2 Coreless inductor model **a** capacitance representation on the spiral inductor, **b** electrical model at high frequencies, **c** electrical model at low frequencies
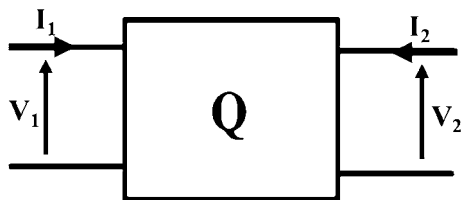

Fig. 3 Two-port network (quadrupole)

L is constant because no magnetic material is used for this inductor and the loss tangent of the substrate is negligible [22]. Capacitances are also constant because

the substrate permittivity is constant on the entire frequency range.

Using impedance matrix of the full inductor, the model parameters L, C_1, C_2 and C_{12} can be determined.

$$Y_{11} = \frac{1}{r_{(f)} + jL2\pi f} + j(C_1 + C_{12})2\pi f \tag{4}$$

$$Y_{12} = Y_{21} = -\left(\frac{1}{r_{(f)} + jL2\pi f} + jC_{12}2\pi f\right) \tag{5}$$

$$Y_{22} = \frac{1}{r_{(f)} + jL2\pi f} + j(C_2 + C_{12})2\pi f \tag{6}$$

These four constant parameters are determined as shown in Fig. 4. In the linear part of the curve (slope of -20 dB/decade) that represents the evolution of the Y_{12}-parameter versus frequency, one can state that Y_{12} is purely inductive. In these conditions,

$$L\omega = \frac{1}{|Y_{12}|_{dB}} \tag{7}$$

and

$$L = \frac{10^{-Y_{12}dB/20}}{2\pi f} \tag{8}$$

The resonance frequencies of Y_{12}, Y_{11} and Y_{22} admittances allow the capacitances C_{12}, C_1 and C_2 respectively to be calculated. The frequency resonance of an LC network is related to L and C values:

$$f_0 = 1/2\pi\sqrt{LC} \tag{9}$$

In these conditions, capacitances are expressed below:
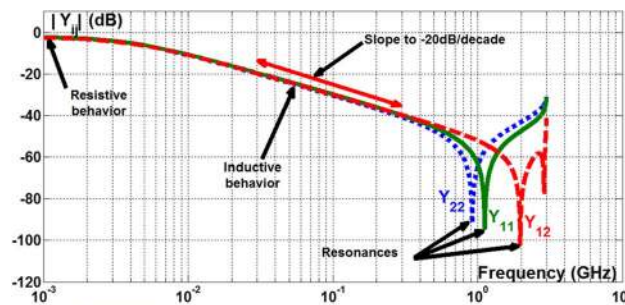
$$C_{12} = \frac{1}{f_{0Y_{12}}^2 4\pi^2 L} \tag{10}$$

Fig. 4 Simulated Y_{ij} admittance curves

$$C_{12} + C_1 = \frac{1}{f_{0_{Y_{11}}}^2 \, 4\pi^2 L} \tag{11}$$

$$C_{12} + C_2 = \frac{1}{f_{0_{Y_{22}}}^2 \, 4\pi^2 L} \tag{12}$$

f_{0Y12}, f_{0Y11}, f_{0Y22} are parallel resonance frequencies of Y_{12}, Y_{11} and Y_{22} parameters.

2.2 Accuracy and frequency range

A careful consideration should therefore be given to the choice of the frequency domain in order to determine the $r_{(f)}$ value. Calculation of Y_{ij} parameters using scattering parameters can lead to significant errors. In order to illustrate this problem, Y_{12} parameter has been calculated with inaccurate S_{ij} parameters. Figure 5 shows Y_{12} parameter that was calculated with 3 sets of different S_{ij} parameters: S_{ij} (the correct value), $0.99S_{ij}$ (with an error of 1%) and $0.95S_{ij}$ (with an error of 5%).

Important errors can be observed at low frequencies that means Y_{12} parameter has not to be used in this frequency range.

So, the resistance can be measured with an LRC-meter or calculated.

The resistance **$r_{(f)}$** is frequency dependent and has to be determined in 3 frequency domains:

1. at very low frequencies (or DC) without using Y_{12}
2. at medium frequencies (capacitive couplings are negligible) and the impedances r and Lω are in the same order of magnitude (before the slope of -20 dB/decade)
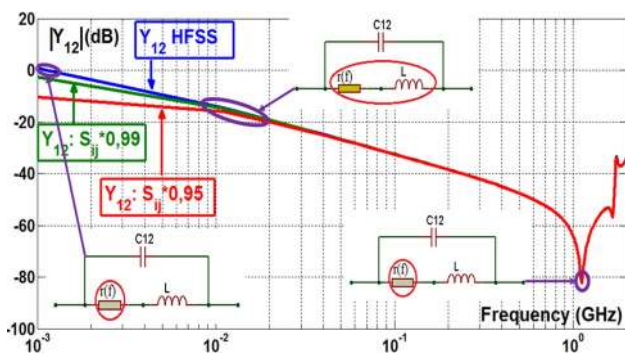3. at resonant frequencies i.e. high frequencies.

2.2.1 At very low frequencies (or DC)

The very low frequencies resistance can be either calculated or measured. If the 3D finite element analysis software is not able to give an accurate value at low frequencies, the DC resistance can be calculated using [10]:

$$R_{DC} = \frac{\rho l}{S} \tag{13}$$

where ρ is the copper resistivity, l the length of the wire and S the copper section.

LCR-meter or Impedance–meter are suitable equipment to measure a low frequency resistance by using a 4-wires method.

2.3 At low-medium frequencies

Figure 6 shows the equivalent circuit for Y_{12} parameter in this frequency range. At low-medium frequencies capacitive couplings (C_1, C_2 and C_{12}) are negligible and only consider the two elements $r_{(f)}$ and L can be considered.

So, the expression of the Y_{12} parameter is:

$$Y_{12} = -\frac{1}{r_{(f)} + jL\omega} \tag{14}$$

From Eq. (14), the real part of this expression is equal to:

$$Real(Y_{12}) = -\frac{r_{(f)}}{r_{(f)}^2 + L^2(2\pi f)^2} \tag{15}$$

In order to simplify the previous expression, write out the following equation:
$\alpha = Real(Y_{12})$
Then, the equation becomes:

$$\alpha r^2 + r + \alpha L^2 \omega^2 = 0 \tag{16}$$

The discriminant of this equation always being positive, two real solutions exist:

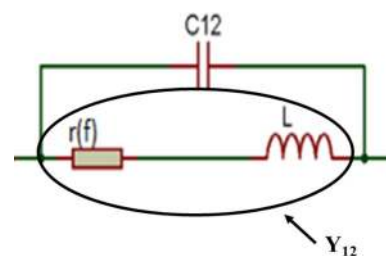$$r_1 = \frac{-1 - \sqrt{1 - 4\alpha^2 L^2 \omega^2}}{2\alpha} \tag{17}$$

Fig. 5 Y_{12} versus frequency: accuracy and frequency range

Fig. 6 Y_{12} equivalent circuit model at low-medium frequencies

$$r_2 = \frac{-1 + \sqrt{1 - 4\alpha^2 L^2 \omega^2}}{2\alpha} \tag{18}$$

In order to determine the right solution, it is necessary to express the two solutions depending on the frequency.

$\Rightarrow$*At low frequencies* $4\alpha^2 L^2 \omega^2 \rightarrow 0$ *that implies:*

$$r_1 = \frac{-1 - \sqrt{1}}{2\alpha} \tag{19}$$

$r_1 = -1/\alpha$ is the right solution and $r_2 = \frac{-1+\sqrt{1}}{2\alpha} = 0$ is not the solution.

$\Rightarrow$*At low-medium frequencies* $L\omega \gg r$, *then*

$$\alpha = \frac{-r}{L^2\omega^2} \tag{20}$$

that implies:

$$r_2 = \frac{-1 + \sqrt{1 - 4\left(\frac{-r}{L^2\omega^2}\right)^2 L^2 \omega^2}}{2\alpha} = \frac{-1 + \sqrt{1 - 4\frac{r^2}{L^2\omega^2}}}{2\alpha} \tag{21}$$

The limited development of $\sqrt{1-\varepsilon}$ is $1 - \varepsilon/2$, then

$$r_2 = \frac{-1 + \left[1 - 4\frac{r^2}{L^2\omega^2} * \frac{1}{2}\right]}{2\alpha} \Rightarrow r_2 = \frac{-2\frac{r^2}{L^2\omega^2}}{2\frac{-r}{L^2\omega^2}} \tag{22}$$

$r_2 = r$ is the right solution and r_1 is not the right solution.

Thus, for low-medium frequencies, the physical solution of this quadratic equation is given by

$$r = \frac{-1 + \sqrt{1 - 4\alpha^2 L^2 (2\pi f)^2}}{2\alpha} \tag{23}$$

2.3.1 At resonant frequencies i.e. high frequencies

At high frequencies no parameter can be neglected. In these conditions, it is very difficult to extract the r value except at the resonant frequency of each Y-parameter. Indeed at the resonant frequency the magnitude of the Y-parameter curve only depends on r value. By using a curve fitting procedure, the r value at the resonant frequency can be determined.

The presented method which consists in determining the $r_{(f)}$ serial resistance in 3 different frequency ranges, has been applied to different coreless inductors.

3 Devices and manufacturing, simulation and measurement

3.1 Devices under test

Many inductors were manufactured by changing different parameters such as number of turns (**N** from 1 to 15), ribbon width (**W** from 100 to 400 µm) and space width (**S** from 50 to 400 µm). Figure 7 illustrates the main dimensions of coreless inductors.

For instance different space widths between turns allow the influence of the distance between turns on proximity effects to be studied. All the devices were manufactured on alumina substrate (Al$_2$O$_3$). At studied frequencies (below GHz) this material exhibits no losses (tg $\delta < 10^{-3}$ [22]). It can be considered as perfect. In these conditions only the relative permittivity ε_r of the substrate is considered for simulation. Figure 8 shows a picture of some fabricated devices. Different square spirals with a ground plane were manufactured in order to use Ground Signal Ground (GSG) probe for the device characterization.

3.2 Inductor manufacturing

The process concerns copper deposition, photolithography and wet etching to obtain the final pattern of the square spiral inductor.

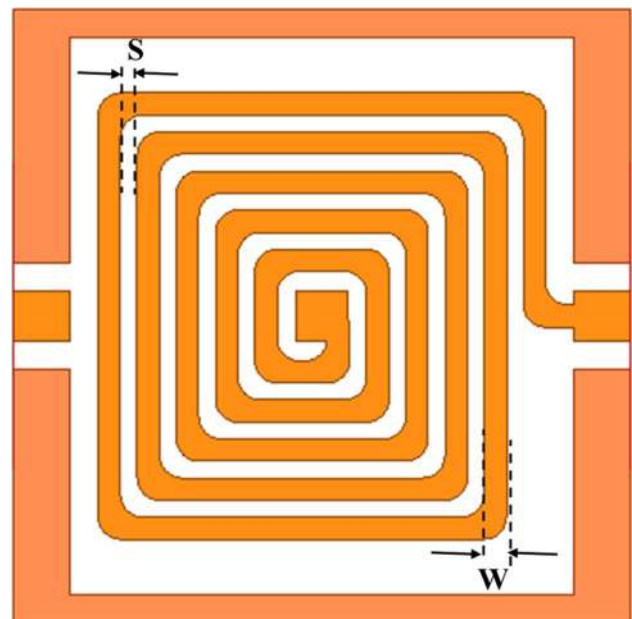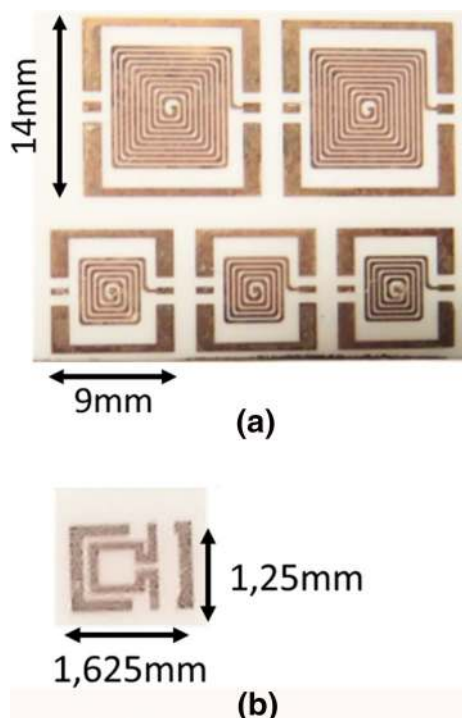First of all, a copper layer is deposited with a thickness chosen according to the desired device (usually

Fig. 7 Main dimensions of inductors

Fig. 8 Coreless inductors on alumina substrate **a** inductors with 5 and 10 turns, **b** inductor with 1 turn

between 1 and 20 μm). The conductive material (copper) deposited by RF sputtering is chosen for its high electrical conductivity.

The spiral pattern manufacturing is obtained in a clean room by conventional photolithography techniques that can be summarized succinctly as follow:

- Deposition of a photoresist layer by spin coating (SPR 505).
- Annealing at 110 °C using a hot plate for 90 s.
- Insulation during 12 s.
- Second annealing at 110 °C using an oven for 90 s.
- Developing and removing photoresist layer
- Final annealing at 110 °C using an oven for 4 min.

These steps are followed by wet etching in a solution of ferric chloride at 30 °C. The etching time depends on the concentration of ferric chloride, the temperature of the solution and the thickness of the deposited layer. The etching is generally performed in less than 1 min. In order to prevent any oxidation of the copper ribbons a thin gold layer is electroplated on the copper ribbons.

The last step concerns the connection between the inner central pad and the outer one. This connection is performed by using a wire bonding.
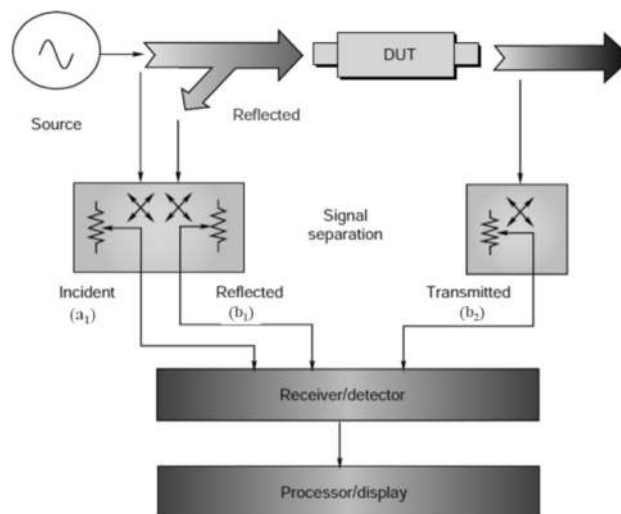
Fig. 9 Operating principle diagram of the vector network analyser

3.3 Simulation

Simulations are carried out with HFSS, a 3-D full-wave, frequency domain electromagnetic field solver based on the finite element method (FEM). In order to take into account both skin and proximity effects the copper conductors are also meshed in volume. Moreover the device under test is positioned in an important air box. Boundary conditions are defined as a perfect conductor (Perfect E).

3.4 Measurement set-up

Measurements are performed using a vector network analyzer (Rohde&Schartz ZVA67) and a probing system. This equipment allow the devices to be characterized on a broad band frequency (10 MHz to 2 GHz). The operating principle of the vector network analyzer consists in emitting a sinusoidal signal with constant amplitude and variable frequency on the device to determine the dispersion parameters S of this device (Fig. 9).

This diagram explains the principle for measuring S_{11} and S_{21} parameters. In order to obtain the complete dispersion matrix, the source is activated in the second port. By switching the source on both ports, the reflection and transmission parameters S_{11}, S_{21}, S_{12} and S_{22} can be measured.

In order to minimize measurement errors, S_{ij} parameters are measured with a prior OSTL (Open Short Thru Load) calibration. This calibration allows an impedance reference at the end of the probe to be equal to 50 Ω.

The measurement results are expressed as S_{ij} parameters. To analyze these results, intermediate relations are used to obtain Y_{ij} parameters [15].

Fig. 10 Measured series resistance $r_{(f)}$ versus frequency
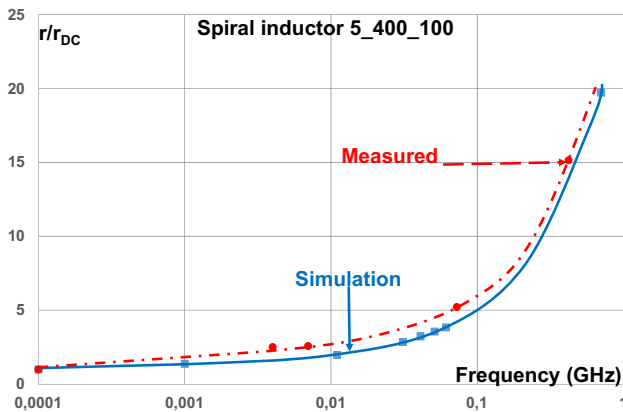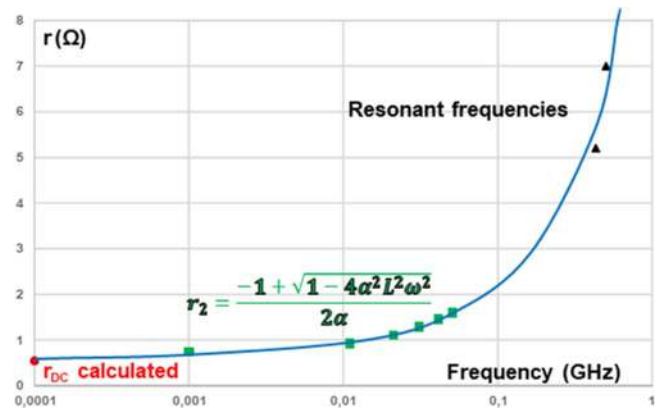
Fig. 11 Comparison between extracted resistances from simulation and measurement for inductor 5 turns_400 μm ribbon width_100 μm turn spacing
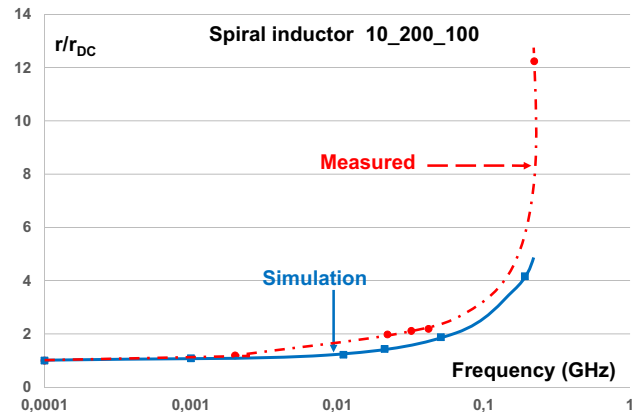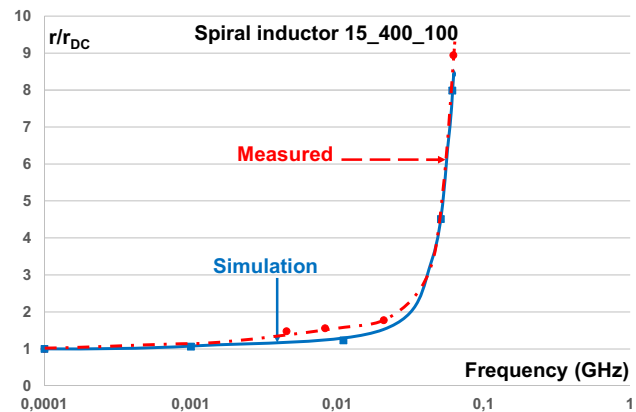

Fig. 12 Comparison between extracted resistances from simulation and measurement for inductor 10 turns_200 μm ribbon width 100 μm turn spacing

4 Results

In order to illustrate our approach, Fig. 10 shows an example of the variation of the resistance $r_{(f)}$ versus frequency. This curve is drawn for a coreless inductor which exhibits the following characteristics: – number of turns (N): 5—square spiral–copper thickness (e): 5 μm—ribbon width (W): 400 μm—space width (S): 50 μm. This device is noted 5-400-50. The two high-frequency points marked by a triangle were obtained from the resonances of the parameters Y_{11} and Y_{22}.

4.1 Comparison between simulation and measurement

Comparisons between extracted resistances from both simulation and measurement are shown in Figs. 11, 12, 13 and 14 for four inductors which exhibit 1, 5, 10 and 15 turns. The dashed curves show the ratio $r_{(f)}/r_{DC}$

Fig. 13 Comparison between extracted resistances from simulation and measurement for inductor 15 turns_400 μm ribbon width 100 μm turn spacing
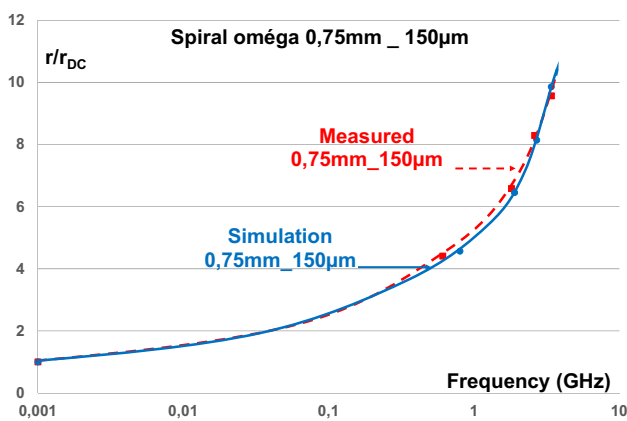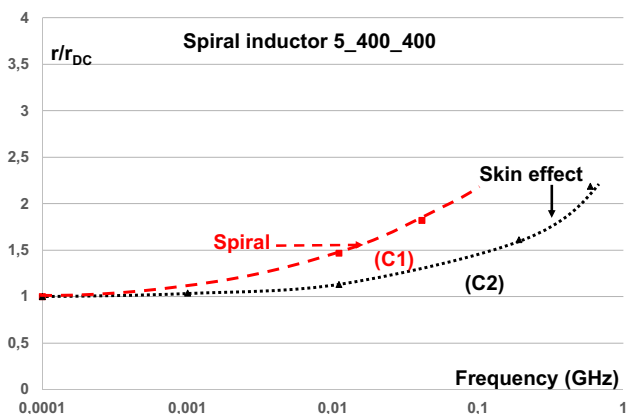
Fig. 14 Comparison between extracted resistances from simulation and measurement for inductor 1 turn_0.75 mm length _150 μm ribbon width

determined from measurements while the solid curves show $r_{(f)}/r_{DC}$ determined from simulation (HFSS).

A good agreement between simulated and measured curves is observed for each inductor. Thus, these results allow the developed method to be validated. On the other hand, these results show that either simulated curves or measured can be used for determine the evolution of the resistance depending on the frequency.

4.2 Method for separating skin effects and proximity effects

In order to illustrate skin effects and proximity effects, Fig. 15 compares two normalized resistance r/r_{DC} as a function of frequency. These two curves correspond to the same device (all geometric parameters are identical).

The curve (C_1) is obtained by using our approach in order to take into account all winding high-frequency effects.

The curve (C_2) shows the increase of the ratio $r_{(f)}/r_{DC}$ which is only due to skin effects (proximity effects are not taken into account). The expression given by Yue [6] (1) is used to calculate $r_{(f)}$:

From Fig. 15 curve C_1 exhibits a higher increase than curve C_2 which only considers skin effects. This confirms that both skin and proximity effects are taken into account in our novel method.

In order to validate the previous assumption, Fig. 16 shows the ratio $r_{(f)}/r_{DC}$ versus frequency for different turn spacing, the other parameters are kept identical:
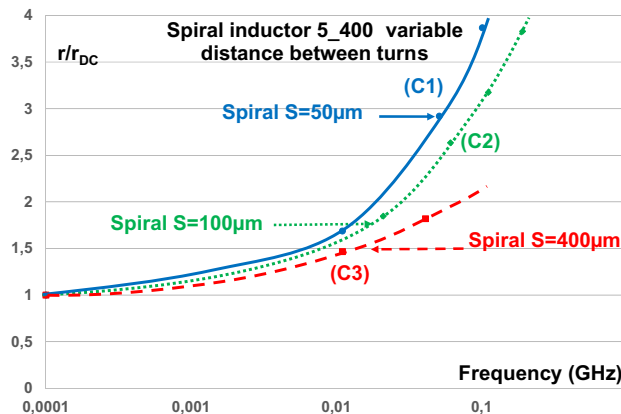
- Curve (C_1) the turn spacing is equal to 50 μm,
- Curve (C_2) the turn spacing is equal to 100 μm,
- Curve (C_3) the turn spacing is equal to 400 μm

Figure 16 shows that $r_{(f)}/r_{DC}$ ratios depend on turn spacing. The smaller the space between turns is the higher the ratio $r_{(f)}/r_{DC}$ is. That demonstrates proximity effects are taken into account.

In these conditions, skin and proximity effects can be separated as illustrated on Fig. 17.

- The curve (C_1) shows the resistance r_{DC} that can be either measured by using a low frequency equipment such as LCR meter or calculated ($r_{DC} = \rho \frac{l}{S}$)

- The curve (C_2) that only takes into account skin effect is obtained from Yue's expression (1).
- The curve (C_3) taking into account both skin and proximity effects is obtained either from measurement or from simulation.

Fig. 15 $r_{(f)}/r_{DC}$ versus frequency taking into account skin effect (C2) and skin and proximity effects (C1) for inductor 5 turns_ 400 μm ribbon width 400 μm turn spacing

Fig. 16 $r_{(f)}/r_{DC}$ versus frequency taking into account skin and proximity effects for 3 inductors 5 turns_400 μm ribbon width and different turn spacing (50 μm, 100 μm and 400 μm)

Fig. 17 Loss separation for inductor 5 turns_ 400 μm ribbon width 400 μm turn spacing
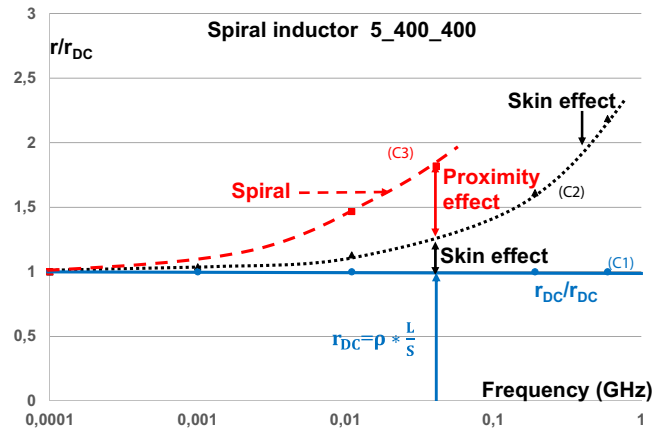
5 Conclusion

In this article, winding loss determination for integrated inductors has been demonstrated. The presented approach is different from those encountered in literature and allows the series resistance from measured or simulated scattering parameters S_{ij} to be determined. Winding losses are taken into account by means of a series resistance which depends on frequency. Simulation and measurements have been carried out and a good agreement is observed. This method allows losses to be separated in two parts: skin effect and proximity effect for coreless inductors.

Compliance with ethical standards

References

1. Dowell PL (1966) Effects of eddy currents in transformer windings. Proc Inst Electr Engin 113(8):1387–1394
2. Ferreira JA (1994) Improved analytical modeling of conductive losses in magnetic components. IEEE Trans Power Electron 9(1):127–131
3. Xi N, Sullivan CR (2003) An improved calculation of proximity-effect loss in high-frequency windings of round conductors. In: Procedings of the IEEE 34th annual conference on power electronics specialist
4. Roßkopf A, Bar E, Joffe C (2014) Influence of inner skin- and proximity effects on conduction in litz wires. IEEE Trans Power Electron 29(10):5454–5461
5. Chen W, Yan Y, Hu Y, Lu Q (2003) Model and design of PCB parallel winding for planar transformer. IEEE Trans Magn 39(5):3202–3204
6. Yue CP, Wong SS (2000) Physical modeling of spiral inductors on silicon. IEEE Trans Electron Devices 47(3):560–568
7. Kuhn WB, Ibrahim NM (2000) Analysis of current crowding effects in multiturn spiral inductors. IEEE Trans Microw Theory Tech 49(1):31–38
8. Lee KK, Bryant C, Törmänen M, Sjöland H (2009) A 65-nm CMOS ultra-low-power LC quadrature VCO. In: Proceedings of the NORCHIP conference
9. Kaluza M, Napieralski A (2008) Frequency sampling approach to the problem of silicon integrated spiral inductors modeling. Bull Pol Acad Sci 56(1):21–27
10. Kuhn WB, Boutz AP (2010) Measuring and reporting high quality factors of inductors using vector network analyzers. IEEE Trans Microw Theory Tech 58(4):1046–1055
11. Harburg DV, Qiu J, Sullivan CR (2012) An improved AC loss model for the optimization of planar-coil inductors. In: IEEE 13th workshop on control and modeling for power electronics
12. Wang N, O'Donnell T, O'Mathuna C (2013) An improved calculation of copper losses in integrated power inductors on silicon. IEEE Trans Power Electron 28(8):3641–3647
13. Abderahim A, Mahamat AT, Chatelon JP, Pietroy D, Capraro S, Rousseau JJ (2016) Approach of copper losses determination in planar windings. Electron Lett 52(12):1050–1052
14. Abderahim A, Mahamat AT, Capraro S, Moungache S, Chatelon JP, Pietroy D, Rousseau JJ (2016) Determination of copper losses from measurement and simulation in planar windings. In: Proceedings of the design, test, integration and packaging of MEMS/MOEMS
15. Frickey DA (1994) Conversions between S, Z, Y, H, ABCD, and T parameters which are valid for complex source and load impedances. IEEE Trans Microw Theory Tech 42(2):205–211
16. Ooi B-L, Dao-Xian X, Kooi P-S, Lin F-J (2002) An improved prediction of series resistance in spiral inductor modeling with eddy current effect. IEEE Trans Microw Theory Tech 50(9):2202–2206
17. Chen J, Liou JJ (2004) On-chip spiral inductors for RF applications: an overview. J Semicond Technol Sci 4(3):149–167
18. Talwalkar NA, Yue CP, Wong SS (2005) Analysis and synthesis of on-chip spiral inductors. IEEE Trans Electron Devices 52(2):176–182
19. Han Y, Cheung G, Li A, Sullivan CR, Perreault DJ (2012) Evaluation of magnetic materials for very high frequency power applications. IEEE Trans Power Electron 27(1):425–435
20. Cao Y, Groves RA, Zamdmer ND, Plouchart JO, Wachnik RA, Huang X, King TJ, Hu C (2020) Frequency-independent equivalent-circuit model for on-chip spiral inductors. In: Proceedings of the IEEE custom integrated circuits conference

21. Mu M, Li Q, Gilham DJ, Lee FC, Ngo KDT (2014) New core loss measurement method for high-frequency magnetic materials. IEEE Trans Power Electron 29(8):4374–4381

22. Rajab KZ, Naftaly M, Linfield EH, Nino JC, Arenas D, Tanner D, Mittra R, Lanagan M (2008) Broadband dielectric characterization of aluminum oxide (Al_2O_3). J Micro Electr Pack 5:101–106